Comparison of node-centered and cell-centered unstructured finite-volume discretizations. Part I: viscous fluxes

Boris Diskin* James L. Thomas† Eric J. Nielsen‡ Hiroaki Nishikawa§
Jeffery A. White¶

Discretization of the viscous terms in current finite-volume unstructured-grid schemes are compared using node-centered and cell-centered approaches in two dimensions. Accuracy and efficiency are studied for six nominally second-order accurate schemes: a node-centered scheme, cell-centered node-averaging schemes with and without clipping, and cell-centered schemes with unweighted, weighted, and approximately mapped least-square face gradient reconstruction. The grids considered range from structured (regular) grids to irregular grids composed of arbitrary mixtures of triangles and quadrilaterals, including random perturbations of the grid points to bring out the worst possible behavior of the solution. Two classes of tests are considered. The first class of tests involves smooth manufactured solutions on both isotropic and highly anisotropic grids with discontinuous metrics, typical of those encountered in grid adaptation. The second class concerns solutions and grids varying strongly anisotropically over a curved body, typical of those encountered in high-Reynolds number turbulent flow simulations. Results from the first class indicate the face least-square methods, the node-averaging method without clipping, and the node-centered method demonstrate second-order convergence of discretization errors with very similar accuracies per degree of freedom. The second class of tests are more discriminating. The node-centered scheme is always second order with an accuracy and complexity in linearization comparable to the best of the cell-centered schemes. In comparison, the cell-centered node-averaging schemes are less accurate, have a higher complexity in linearization, and can fail to converge to the exact solution when clipping of the node-averaged values is used. The cell-centered schemes using least-square face gradient reconstruction have more compact stencils with a complexity similar to the complexity of the node-centered scheme. For simulations on highly anisotropic curved grids, the least-square methods have to be amended either by introducing a local mapping of the surface anisotropy or modifying the scheme stencil to reflect the direction of strong coupling.

I. Introduction

Both node-centered and cell-centered finite-volume discretizations are widely used for complex three-dimensional turbulent simulations in aerospace applications. The relative advantages of the two approaches have been extensively studied in the search for methods that are accurate, efficient, and robust over the broadest possible range of grid and solution parameters. The topic was discussed in a panel session at the 2007 AIAA CFD conference, but a consensus did not emerge. One of the difficulties in assessing the two approaches is that comparative calculations were not completed in a controlled environment, i.e., computations were made with different codes and different degrees of freedom and the exact solutions were not known.

In this paper, we provide a controlled environment for comparing a subset of the discretization elements needed in turbulent simulations, namely that of the viscous discretization. In particular, we consider only Poisson's equation as a model of viscous discretization. We use the method of manufactured solution, so that the exact solution is known, and conduct theoretical and computational studies of both accuracy and efficiency for a range of grids. There

---

[*] National Institute of Aerospace (NIA), 100 Exploration Way, Hampton, VA 23681, USA, Member AIAA bdiskin@nianet.org. Also Department of Mechanical and Aerospace Engineering, University of Virginia, Charlottesville, VA 22904, USA. Supported by NASA Fundamental Aeronautics Program, Supersonics Project, NRA Contract NNL07AA23C (PI: prof. N. K. Yamaleev)

[†] Computational Aerosciences Branch, NASA Langley Research Center, Mail Stop 128, Fellow AIAA, James.L.Thomas@nasa.gov.

[‡] Computational Aerosciences Branch, NASA Langley Research Center, Mail Stop 128, Senior Member AIAA, Eric.J.Nielsen@nasa.gov.

[§] National Institute of Aerospace (NIA), 100 Exploration Way, Hampton, VA 23681, USA, Member AIAA hiro@nianet.org

[¶] Computational Aerosciences Branch, NASA Langley Research Center, Mail Stop 128, Senior Member AIAA, Jeffery.A.White@nasa.gov.

are six main schemes considered: a node-centered scheme, cell-centered node-averaging schemes with and without clipping, and cell-centered schemes with unweighted, weighted, and approximately mapped least-square face gradient reconstruction. Each of the schemes considered are nominally second-order accurate.

The two-dimensional (2D) grids considered range from structured (regular) grids to irregular grids composed of arbitrary mixtures of triangles and quadrilaterals. Highly irregular grids are deliberately constructed through random perturbations of structured grids to bring out the worst possible behavior of the solution. Two classes of tests are considered. The first class of tests involves smooth manufactured solutions on both isotropic and highly anisotropic grids with discontinuous metrics, typical of those encountered in grid adaptation. The second class of tests concerns solutions and grids varying strongly anisotropically over a curved body, typical of those encountered in high-Reynolds number turbulent flow simulations. The properties to be compared are (1) computational complexity (operation count) at equivalent discretization accuracy and (2) efficiency and robustness of iterative solvers.

This paper is the first part from an envisioned series of three papers comparing node centered and cell centered discretizations. The second part will address inviscid fluxes, and the third part will discuss complete Reynolds-Averaged Navier-Stokes formulations.

II. Grid specification

This paper studies finite-volume discretization (FVD) schemes for viscous fluxes on grids that are loosely defined as irregular. There is no commonly accepted definition for irregular grids, so, for clarity, we specify the grid terminology used in this paper.

A grid is classified as *periodic* if it has (1) a periodic node connectivity pattern (i.e., the number of edges per node changes periodically) and (2) a periodic cell distribution (i.e., the grid is composed of periodically repeated combinations of cells). Thus, periodic grids can be analyzed by Fourier analysis. Grids that are derived from periodic grids by a smooth mapping are called *regular* grids. Examples of regular grids include, but are not limited to, grids derived from Cartesian ones: triangular grids obtained by diagonal splitting with a periodic pattern, smoothly stretched grids, skewed grids, smooth curvilinear grids, etc. Grids that cannot be smoothly mapped to a periodic grid are called *irregular* grids. Grids with varying local topology are called *unstructured*, e.g., grids with the number of edges changing from node to node with no pattern.

The regular and irregular grids considered in this paper are derived from an underlying (possibly mapped) Cartesian grid with meshsizes h_x and h_y and the aspect ratio $A = \frac{h_x}{h_y}$; both meshsizes of the underlying grid are assumed to be small, $h_y \ll 1, h_x \ll 1$. Irregularities are introduced *locally* and do not affect grid topology and metrics outside of a few neighboring cells. A local grid perturbation is called *random* if it is independent of local perturbations introduced beyond some immediate neighborhood. For computational grids generated for the reported studies, grid irregularities are introduced in two ways (both local and random): (1) the quadrilateral cells of the underlying grid are randomly split (or not split) into triangles; (2) the grid nodes are perturbed from their original positions by random shifts; the shifts are fractions of a local meshsize.

Six grid types are considered: (I) *regular quadrilateral* (i.e., mapped Cartesian) grids; (II) *regular triangular grids* derived from the regular quadrilateral grids by the same diagonal splitting of each quadrangle; (III) *random triangular grids*, in which regular quadrangles are split by randomly chosen diagonals, each diagonal orientation occurring with probability of half; (IV) *perturbed triangular grids*, which are random triangular grids, with grid nodes perturbed from their initial positions by random shifts; (V) *perturbed quadrilateral grids*, which are quadrilateral grids with randomly perturbed grid nodes; and (VI) *perturbed mixed-element grids*, in which perturbed quadrangles are randomly split or not split by randomly chosen diagonals. Grids of types (III), (IV), and (VI) are irregular because there is no periodic connectivity pattern. Grids of types (IV)-(VI) are irregular because there is no periodic pattern for cell distribution. The representative grids are shown in Figure 1.

Our main interest is in studying accuracy and stability properties of FVD schemes on general irregular (mostly unstructured) grids with a minimum set of constraints. In particular, we do not require any grid smoothness, neither on individual grids nor in the limit of grid refinement. The only major requirement for a sequence of refined grids is to satisfy the *consistent refinement property*. The property requires the maximum distance across the grid cells to decrease consistently with increase of the total number of grid points, *N*. In particular, the maximum distance should tend to zero as $N^{-1/2}$ in 2D computations. For three-dimensional (3D) unstructured grids, the consistent refinement property is studied in Ref.[21]

The locations of discrete solutions are called *data points*. For consistency with the 3D terminology, the 2D cell

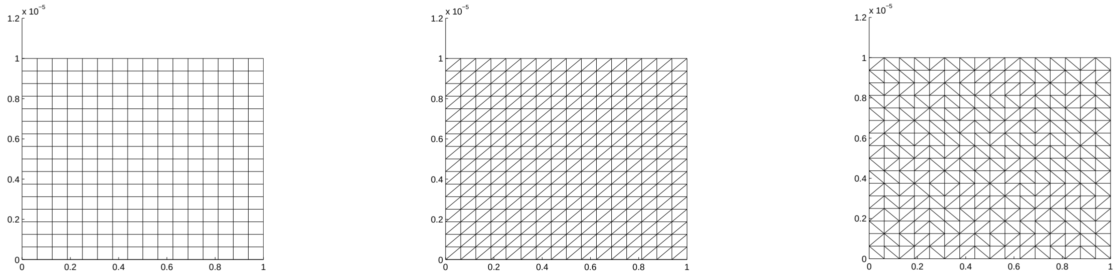

(a) Type (I): Regular quadrilateral grid

(b) Type (II): Regular triangular grid

(c) Type (III): Random triangular grid

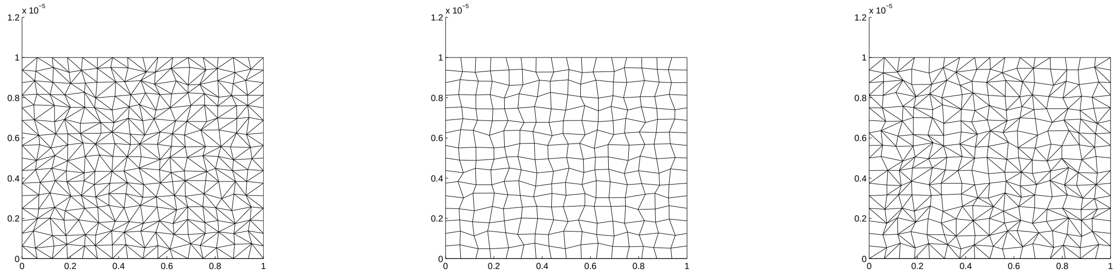

(d) Type (IV): Perturbed triangular grid

(e) Type (V): Perturbed quadrilateral grid

(f) Type (VI): Perturbed mixed grid

Figure 1. Typical regular and irregular grids.

boundaries are called faces, and the term "edge" refers to a line, possibly virtual, connecting the neighboring data points. Each face is characterized by two vectors: (1) the *edge vector*, which connects the data points of the cells sharing the face and (2) the *directed-area vector*, which is normal to the face and has the amplitude equal to the face area. For each cell/face combination, the vectors are directed outward. *Local grid skewness* is measured at a face as the *skew angle* between the edge vector and the directed-area vector; small skew angles correspond to low skewness. On grids with convex cells, the maximum skewness is bounded by $90°$; on more general grids with non-convex cells, the skew angle can approach $180°$. As shown further in the paper, the grid skewness plays a critical role in defining accuracy and stability of FVD solutions.

For most of the computational tests, the random node perturbation in each dimension is defined as $\frac{1}{4}rh$, where $r \in [-1, 1]$ is a random number and h is the local meshsize along the given dimension. With these perturbations, triangular cells in the rectangular geometry are allowed to collapse, i.e., a cell may become a zero-volume cell, albeit with a probability approaching zero. The random perturbations are introduced independently on all grids in grid refinement implying that grids of types (IV)-(VI) are grids with discontinuous metrics, e.g., ratios of neighboring cell volumes and face areas are random on all grids and do not approach unity in the limit of grid refinement.

III. Finite-volume discretization schemes

The considered model problem is the Poisson equation

$$\Delta U = f, \tag{1}$$

subject to Dirichlet boundary conditions; function f is a forcing function independent of the solution. The 2D primal meshes generated for this study are composed of triangular and quadrilateral cells. The FVD schemes are derived from the integral form of a conservation law

$$\oint_{\Gamma} \nabla U \cdot \hat{\mathbf{n}}\, d\Gamma = \iint_{\Omega} f d\Omega, \tag{2}$$

where ∇U is the solution gradient, Ω is a control volume with boundary Γ, and $\hat{\mathbf{n}}$ is the outward unit normal vector. The general FVD approach requires partitioning the domain into a set of non-overlapping control volumes and numerically implementing equation (2) over each control volume.

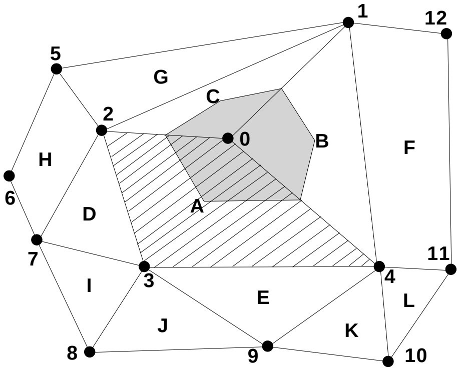

Figure 2. Control-volume partitioning for finite-volume discretizations. Numbers $0-12$ and letters $A-L$ denote grid nodes and primal cell centers, respectively. The control volume for a node-centered discretization around the grid node 0 is shaded. The control volume for a cell-centered discretization around the cell center A is hashed.

Cell-centered and node-centered discretizations are considered. *Cell-centered discretizations* assume solutions are defined at the centers of the primal grid cells with the primal cells serving as the control volumes. The cell center coordinates are typically defined as the averages of the coordinates of the cell's vertexes. *Node-centered discretizations* assume solutions are defined at the primal mesh nodes. For node-centered schemes, control volumes are constructed around the mesh nodes by the median-dual partition: the centers of primal cells are connected with the midpoints of the surrounding faces. These non-overlapping control volumes cover the entire computational domain and compose a mesh that is dual to the primal mesh. Both cell-centered and node-centered control-volume partitions are illustrated in Figure 2.

A. Cell-centered FVD schemes

In cell-centered discretizations, the conservation law (2) is enforced on control volumes that are primary cells. The flux at a face is computed as the inner product of the solution gradient at the face and the directed-area vector. With reference to Figure 2, the gradient, ∇U_{04}, at the face linking nodes 0 and 4 is computed to satisfy two relations:

1. $(\nabla U_{04} \cdot \mathbf{e}_{AB}^{edge}) = \frac{U_B - U_A}{\left|\mathbf{r}_B^c - \mathbf{r}_A^c\right|}$, where $\mathbf{e}_{AB}^{edge} = \frac{\mathbf{r}_B^c - \mathbf{r}_A^c}{\left|\mathbf{r}_B^c - \mathbf{r}_A^c\right|}$ is the edge $[AB]$ unit vector; U_A and U_B are the solutions defined at the cell centers; $\mathbf{r}_A^c$ and $\mathbf{r}_B^c$ are the cell-center coordinate vectors.
2. $(\nabla U_{04} \cdot \mathbf{e}_{04}^{face}) = \left|\nabla U^{face}\right|$, where $\mathbf{e}_{04}^{face} = \frac{\mathbf{r}_4^n - \mathbf{r}_0^n}{\left|\mathbf{r}_4^n - \mathbf{r}_0^n\right|}$ is the face unit vector and $\left|\nabla U^{face}\right|$ is the solution derivative computed along the face $[0,4]$; $\mathbf{r}_i^n$ is a coordinate vector of the node i.

The cell-centered FVD schemes considered in this paper differ only in computing $\left|\nabla U^{face}\right|$.

1. Cell-centered node-averaging FVD schemes

In the node-averaging (NA) schemes, the solution derivative along the face is computed as the divided difference between the solution values reconstructed at the nodes from the surrounding cell centers. With respect to Figure 2, the solution at the node 0 is reconstructed by averaging solutions defined at the cell centers A, B, and C. The solution reconstruction proposed in[13, 18] and used in[6] is an averaging procedure that is based on a constrained optimization to satisfy some Laplacian properties. The scheme is second-order accurate and stable when the coefficients of the introduced pseudo-Laplacian operator are close to 1. It has been shown in[10] that this averaging procedure is equivalent to an unweighted least-square linear fit. The gradient is resolved from the derivative along the face and the derivative along the edge connecting the cell centers across the face. For the face $[0, 4]$, the face derivative is computed using solutions reconstructed by node averaging at the nodes 0 and 4; the edge derivative is computed using solutions at cell centers A and B.

On highly stretched and deformed grids, some coefficients of the pseudo-Laplacian may become negative or larger than 2, which has a detrimental effect on stability and robustness.[2,3] Holmes and Connell[13] proposed to enforce stability by clipping the coefficients between 0 and 2. The NA schemes with clipping represent a current standard in practical computational fluid dynamics (CFD) for applications involving cell-centered finite volume formulations. As shown further in the paper, clipping seriously degrades the solution accuracy.

The computational stencils of NA schemes are very large, so direct relaxation of the full linearization operator is prohibitively expensive. Defect-correction iterations are widely used as a practical solution method. A common driver used for defect-correction iterations is an edge-based thin-shear-layer (TSL) FVD scheme. Although the TSL schemes are not accurate on general grids (accuracy of TSL FVD schemes is zeroth order on general grids), the defect-correction method is efficient on grids with low skewing. As shown in Section IX, efficiency and stability of defect-correction methods with TSL drivers degrade for grids with high skewing.

2. *Cell-centered face-least-square scheme*

An alternative cell-centered scheme relies on a face-based least-square method. First, a gradient is reconstructed within a face using a least-square procedure. The derivative along the face is computed by inner product of the reconstructed face gradient with the face tangent (unit) vector.

In this paper, we consider two approaches to determine stencils for the least-square linear fit. The stencil of type (A) includes the two prime cells sharing the face and their face neighbors that share at least one of the face nodes. A more compact stencil of type (B) typically involves the two prime cells and two auxiliary cells; one for each prime cell. The auxiliary cell is chosen from the pool of the cells sharing the nodes of the face as the cell closest to the prime cell, but not its face neighbor. The stencil of type (B) is important for discretizations on high-aspect-ratio grids of types (I)-(III) to represent correctly the direction of the strong coupling.

Three types of least-square methods are considered. In Cartesian coordinates, both weighted (FWLSQ) and unweighted (FULSQ) least-square methods are considered. In the FWLSQ method, the contributions to the minimized functional are weighted with weights inversely proportional to the distance from the face center; in the FULSQ method, all contributions are equally weighted. For the gradient approximation in regions with curvature, an additional approximate mapping (FAMLSQ) method is introduced. The method uses the distance function that is defined as the distance to the nearest boundary and normally available in practical schemes.

B. Node-centered FVD scheme

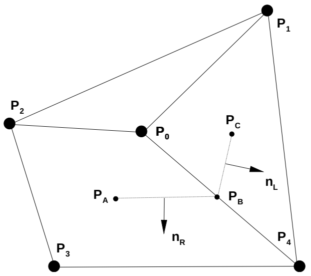

Figure 3. Illustration of gradient reconstruction for viscous terms on mixed grids with median-dual partition.

The second-order accurate node-centered FVD scheme illustrated by Figure 3 represents a standard CFD approach to node-centered viscous discretizations. The scheme approximates the integral flux through the dual faces adjacent to the edge $[P_0, P_4]$ as

$$\int\limits_{ABC} \nabla U \cdot \hat{\mathbf{n}}\, d\Gamma = \nabla U^R \cdot \mathbf{n_R} + \nabla U^L \cdot \mathbf{n_L}. \tag{3}$$

The gradient is reconstructed separately at each dual face as follows.

For the triangular element contribution, the gradient is determined from a Green-Gauss evaluation at the primal-grid element,

$$\nabla U^L = \overline{\nabla U}_{014}. \tag{4}$$

The gradient overbar denotes a gradient evaluated by the Green-Gauss formula on the primal cell identified by the point subscripts. With fully-triangular elements, the formulation is equivalent to a Galerkin finite element scheme with a linear basis function.[1,2] On triangular grids of types (II) and (III) in rectangular geometries, the formulation recovers the five-point Laplacian stencil of the type (I) grids, independent of aspect ratio.

For the quadrilateral element contribution, the gradient is evaluated as

$$\nabla U^R = \overline{\nabla U}_{0234} + \left[|\nabla U^E| - \overline{\nabla U}_{0234} \cdot \mathbf{e}_{04}\right] \mathbf{e}_{04}, \tag{5}$$

where

$$|\nabla U^E| = \frac{U_4 - U_0}{|\mathbf{r}_4^p - \mathbf{r}_0^p|} \tag{6}$$

is the edge gradient computed at the median P_B of the edge $[P_0, P_4]$, U_i and $\mathbf{r}_i^p$ are the solution and the coordinate vector of the node P_i, and

$$\mathbf{e}_{04} = \frac{\mathbf{r}_4^p - \mathbf{r}_0^p}{|\mathbf{r}_4^p - \mathbf{r}_0^p|} \tag{7}$$

is the unit vector aligned with the edge $[P_0, P_4]$. Note that for grids with dual faces perpendicular to the edges, the edge-gradient, $|\nabla U^E|$, is the only contributor. This approach to the gradient reconstruction is used to decrease the scheme susceptibility to odd-even decoupling.[9,11] It has been shown in[4,21] that the scheme possesses second-order accuracy for viscous fluxes on general mixed-element grids.

IV. Complexity of discretization stencils

The size of the stencil for the viscous discretization is examined for 2D and 3D cell-centered and node-centered FVD schemes. Estimates are made for Cartesian meshes split into triangular and tetrahedral elements and neglecting any boundary effects. Estimates are compared to a numerical calculation on an actual 3D turbulent viscous grid that include boundary effects.

In two dimensions, two splittings of the Cartesian grid are considered. The first splits each quadrilateral cell with a diagonal oriented in the same direction. The second splits the cells with diagonals of face-adjacent quadrilaterals oriented in the opposite direction. The second splitting is slightly more analogous to the 3D splitting. In three dimensions, half of the grid nodes have 18 incident edges (32 incident tetrahedra) and half have 6 incident edges (8 incident tetrahedra). Each of the tetrahedra interior to an originally-hexahedral cell is defined by four nodes, each with 18 incident edges. Each of the four surrounding tetrahedra within an originally-hexahedral cell is defined by three nodes with 18 incident edges and 1 node with 6 incident edges. For reference, Table 1 shows the average and maximum number of edges, n_{edge}, connecting to a grid node. The average number of connecting edges sets the stencil size for the node-centered scheme as $s = n_{edge} + 1$. The number of connecting edges is also an important factor in the NA schemes because the values in the control volumes faces are computed from cell-centered data averaged to the grid nodes.[7]

Dimension	n_{edge} (Average)	n_{edge} (Maximum)
2D	6	8
3D	12	18

Table 1. Edges connecting to a grid node in the split Cartesian grids.

Table 2 shows stencil-size estimates for 2D triangular grids. There is a slight difference in the estimates from the two splittings (entries separated by slashes in the table), depending on the diagonalization pattern. The NA stencil is the largest. The face least-square (LSQ) stencil is estimated for the approach (A).

Table 3 shows stencil-size estimates for 3D tetrahedral grids. The NA stencil is again largest. The face least-square stencil is only slightly larger than the stencil of the node-based discretization, in both estimation and computation. The discretization complexity of face LSQ stencils of type (B) is even smaller.

Node-centered	Cell-centered NA	Cell-centered face LSQ
7	13/16	10/9

Table 2. Size of the viscous stencil for 2D discretizations with triangular elements.

	Node-centered	Cell-centered NA	Cell-centered face LSQ
Estimate	13	79	15
Numerical	14	69	15

Table 3. Average size of the viscous stencil for 3D discretizations with tetrahedral elements.

V. Analysis methods

A. Method of manufactured solution

Accuracy of FVD schemes is analyzed for known exact or manufactured solutions. The forcing function and boundary values are found by substituting this solution into the Poisson equation with Dirichlet boundary conditions. The discrete forcing function is defined at the data points.

1. Discretization error

The main accuracy measure is the *discretization error*, E_d, which is defined as the difference between the exact discrete solution, U^h, of the discretized equations (2) and the exact continuous solution, U, to the differential equation (1)

$$E_d = U - U^h; \tag{8}$$

U is sampled at data points.

2. Truncation error

Another accuracy measure commonly used in computations is *truncation error*. Truncation error, E_t, characterizes the accuracy of approximating the differential equation (1). For finite differences, it is defined as the residual obtained after substituting the exact solution U into the discretized differential equations.[12] For FVD schemes, the traditional truncation error is usually defined from the time-dependent standpoint.[20,22] In the steady-state limit, it is defined (e.g., in[8]) as the residual computed after substituting U into the normalized discrete equations (2),

$$E_t = \frac{1}{|\Omega|}\left[-\iint\limits_{\Omega} f^h \, d\Omega + \oint\limits_{\Gamma} \left(\nabla U \cdot \hat{\mathbf{n}} \right) \, d\Gamma \right], \tag{9}$$

where $|\Omega|$ is the measure of the control volume,

$$|\Omega| = \iint\limits_{\Omega} d\Omega, \tag{10}$$

f^h is an approximation of the forcing function f on Ω, and the integrals are computed according to some quadrature formulas. Note that convergence of truncation errors is expected to show the order property only on regular grids; on irregular grids, it has been long known that the design-order discretization-error convergence can be achieved even when truncation errors exhibit a lower-order convergence or, in some cases, do not converge at all.[8,14,15]

3. *Accuracy of gradient reconstruction*

Yet another important accuracy measure is the accuracy of gradient approximation at a control-volume face. For second-order convergence of discretization errors, the gradient is usually required to be approximated with at least first order. For each face, accuracy of the gradient is evaluated by comparing the reconstructed gradient, ∇_r, with the exact gradient, ∇_{exact}, computed at the face center. The accuracy of gradient reconstruction is measured as the relative gradient error:

$$E_{\text{rel}} = \frac{\|\epsilon\|}{\|G\|}, \tag{11}$$

where functions ϵ and G define face-wise amplitudes of the gradient error and the exact gradient, respectively,

$$\epsilon = |\nabla_r U^h - \nabla_{\text{exact}} U|, \qquad \text{and} \qquad G = |\nabla_{\text{exact}} U|; \tag{12}$$

U and U^h are a differentiable manufactured solution and its discrete representation (usually injection) on a given grid, respectively; $\| \cdot \|$ is a norm of interest computed over the entire computational domain.

B. Downscaling test

Recent publications[4,21] introduced a novel practical computational analysis method, downscaling (DS) test, for analyzing convergence of discretization errors on irregular grids. The DS test consists of a series of inexpensive computational experiments that account for local properties of the studied scheme; it is designed to provide estimates for the convergence orders of the discretization errors by comparing errors obtained on different scales. Analysis methods predicting the performance of DS tests have also been developed. While rigorous proofs of estimates for convergence of FVD truncation and discretization errors in realistic computations are still out of reach, the DS test provides an accurate and efficient accuracy assessment on various irregular grids, for various types of solutions and boundary conditions.

C. Computational analysis of discretization errors

On irregular grids derived from regular underlying grids by introducing local irregularities, the total discretization error observed in grid refinement computations is composed of (1) the smooth discretization error and (2) the local discretization error. The *smooth discretization error* is the error that would be observed in grid refinement on the background regular grids. An estimate of the convergence order of the smooth discretization errors can be obtained from observing convergence of averaged truncation errors on the background regular grids. The *local discretization error* is caused by grid irregularities. Its convergence can be directly analyzed in DS tests. For a manufactured solution, the discretization error profile observed on a computational grid is an accurate indicator of which component is dominant: large smooth error component indicates that the main error source is the solution approximation on the background regular grid; a spiky error profile is an indication that a major part of the discretization error is introduced by local grid irregularities.

VI. Isotropic irregular grids with discontinuous metrics

A. Grids and manufactured solution

A sequence of consistently refined grids of either types (IV) or (VI) is generated on the unit square $[0, 1] \times [0, 1]$. Irregularities are introduced at each grid independently, so the grid metrics remain discontinuous on all the grids. The ratio of areas of neighboring faces can be as large as $\frac{6}{\sqrt{2}}$; because a control volume can be arbitrary small, the ratio of the neighboring volumes can be arbitrary high. Isotropic grids randomly generated for this study have 0.01% of cell volumes smaller than $\frac{1}{10}\frac{1}{N^2}$; the total number of grids nodes is $(N+1)^2$; about 0.006% of interior faces have the skew angle larger than 70°. The effective meshsize, h_e, is computed as the L_1 norm of square roots of the control volumes.

B. Gradient reconstruction accuracy

The accuracy of gradient reconstruction for isotropic irregular grids is first order for all methods,[5] which is sufficient for second-order discretization accuracy. As an example, the gradient reconstruction tests are performed for the

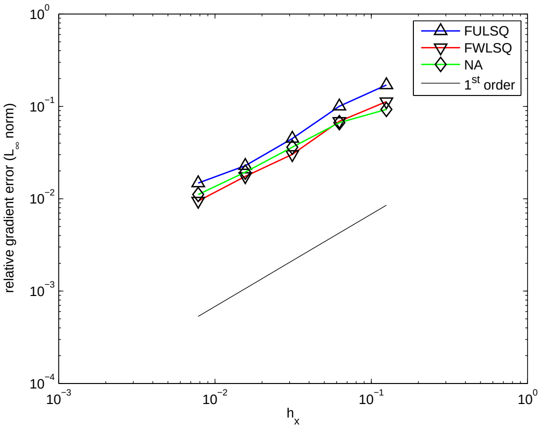

Figure 4. Accuracy of gradient reconstruction on isotropic irregular grids with discontinuous metrics

manufactured solution $U = \sin(\pi x + 2\pi y)$. For both node-centered and cell-centered formulations, gradients are reconstructed within the control-volume face. Figure 4 shows convergence of the L_∞ norm of relative gradient errors on a sequence of refined grids of type (IV). Only cell-centered schemes are shown. The gradients are reconstructed by the FULSQ and FWLSQ methods and by the NA method without clipping. Face-based least-square methods use stencils of type (A).

C. Convergence of truncation and discretization error

The numerical tests evaluating convergence of truncation and discretization errors are performed with Dirichlet boundary conditions specified from the manufactured solution $U = \sin(\pi x + 2\pi y)$ and imposed on all cells linked to the boundary. Figure 5 shows convergence of the L_∞ norms of truncation and discretization errors for the three cell-centered formulations on grids of type (IV). As predicted in,[4,21] truncation errors do not converge on irregular grids in any norm. Discretization errors converge with second order for all the three formulations considered.

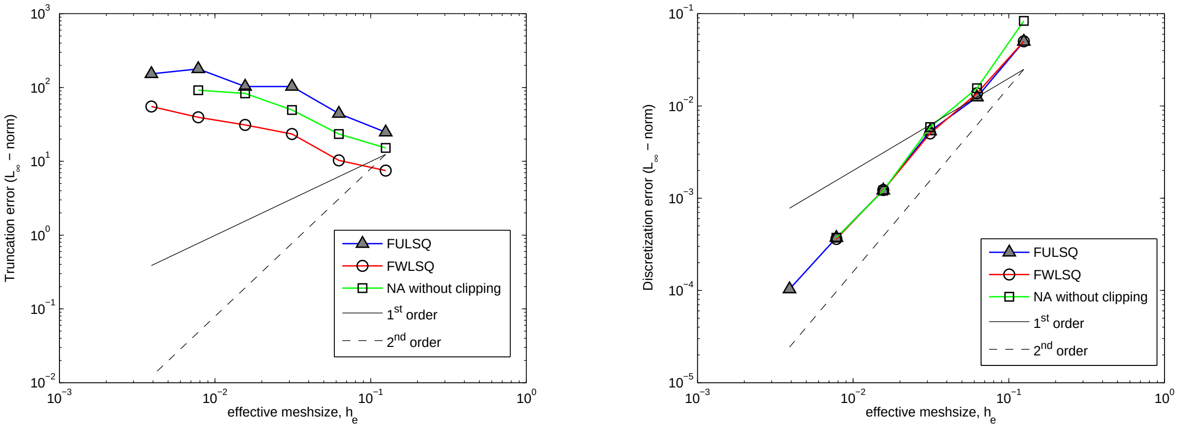

(a) Truncation Errors

(b) Discretization Errors

Figure 5. Convergence of truncation and discretization errors on type (IV) random triangular grids with discontinuous metrics.

Another series of tests is performed to compare the relative accuracy of cell-centered and node-centered schemes on the same consistently refined mixed-element grids of type (VI). For mixed-element grids, approximately half of the cells are randomly split. Dirichlet boundary conditions are specified from the manufactured solution $U =$

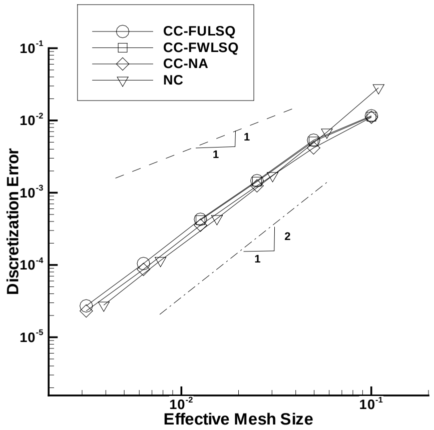

Figure 6. Discretization error convergence on type (VI) mixed-element grids with discontinuous metrics. Prefix CC denotes cell-centered scheme; NC denotes the node-centered scheme. CC-NA scheme without clipping is used.

$\sin(2\pi x + 2\pi y)$. Figure 6 demonstrates convergence of the L_1-norm of the discretization errors. Note that on these mixed-element grids the number of the cells is about 50% larger than the number of nodes. The discretization errors of the cell-centered and node-centered FVD schemes are almost over-plotted, indicating a similar accuracy per degree of freedom, which implies better accuracy for the cell-centered FVD schemes on the same grids, as expected.

D. Effects of clipping

The tests reported in this section are performed for NA schemes and demonstrate detrimental effects of clipping on accuracy of gradient approximation and on the discretization accuracy. The accuracy is evaluated for the manufactured solution $U = \sin(2\pi y)$. Dirichlet boundary conditions over-specified from the manufactured solution are imposed at all control volumes connecting to the boundary. Considered irregular grids of type (IV) with discontinuous metrics are derived from underlying isotropic (unit aspect ratio) Cartesian grids covering the unit square. Figure 7(a) shows an example of an isotropic random triangular grid of type (IV) with 17^2 nodes; nodes where clipping occurs in reconstruction are circled; about 7% of the interior nodes are clipped.

1. Gradient approximation accuracy

The computational gradients are evaluated within interior faces. At each interior face, the normal and tangential components of the computational gradient are computed and compared with the exact-gradient components at the face center. Figure 7(b) shows the maximum norm of the deviation between the computational and the exact-gradient components. The results indicate that the face gradient computed by the NA scheme with clipping does not approximate the exact gradient. The solution of the NA scheme without clipping provides a first-order accurate gradient approximation. Although not shown, the FULSQ and FWLSQ schemes also provide first-order accurate face-gradient approximations.

2. Discretization errors

Figure 8 exhibits convergence of discretization errors. The no-clipping NA scheme demonstrates second-order convergence; convergence of the NA scheme with clipping appears as second order on the coarse grids, but then degrades to the zeroth order. Although not shown, the L_∞ norms of discretization errors converge with the same orders as the corresponding L_1 norms. Inspection of the discretization error profile shows that clipping greatly affects the smooth-error component. Plots of the discretization-error surfaces sliced along the y direction at $x = \frac{1}{2} - \frac{h_0}{4}$ are shown in Figures 9(a) and 9(b) for a grid with 257^2 nodes; the figures display discretization errors at the centers of the cells crossed by the slice versus the y coordinate of the cell centers. For the scheme with clipping, the smooth error is dominant. In fact, for the NA scheme with clipping, the results of a DS test with the focal point at $(x, y) = (0.3, 0.3)$

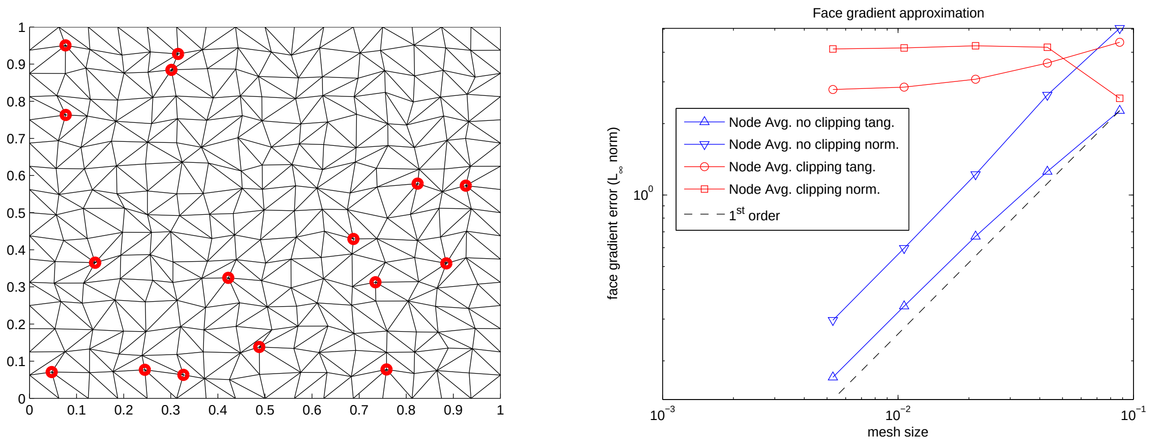

(a) Random triangular grid with 17^2 nodes. Clipped nodes are circled.

(b) Relative gradient error (L_∞ norm)

Figure 7. Gradient approximation accuracy of NA schemes on isotropic irregular triangular grids with discontinuous metrics

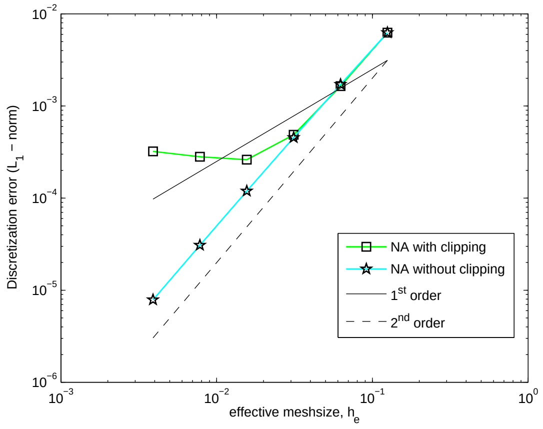

Figure 8. Convergence of NA schemes on isotropic irregular triangular grids with discontinuous metrics

(Figure 10) show that the local errors converge at least with the first order. For the NA scheme without clipping, amplitudes of the smooth and local error components are comparable; both converge with the second order.

VII. Anisotropic irregular grids with discontinuous metrics

In this section, we study FVD schemes on irregular stretched grids generated on rectangular domains. Specifically, a sequence of consistently refined stretched grids is generated on the unit square $[0, 1] \times [0, 1]$ in the following 3 steps.

1. A background regular rectangular grid with $(N+1)^2$ nodes and the horizontal mesh spacing $h_x = \frac{1}{N}$ is stretched toward the horizontal line $y = 0.5$. The coordinates of the horizontal grid lines in the top half of the domain are defined as

$$y_{\frac{N}{2}+1} = 0.5; \qquad y_j = y_{j-1} + \hat{h_y}\beta^{j-\left(\frac{N}{2}+1\right)}, \qquad j = \frac{N}{2}+2, \frac{N}{2}+3, \ldots, N, N+1. \tag{13}$$

Here $\hat{h_y} = \frac{h_x}{A}$ is the minimal mesh spacing between the vertical lines; $A = 1000$ is fixed maximal aspect ratio;

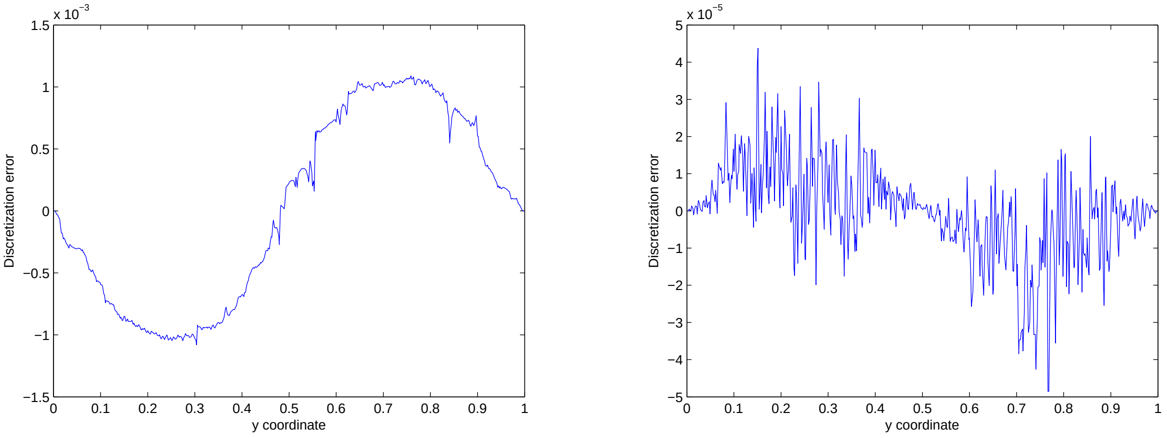

(a) Node averaging scheme with clipping

(b) Node averaging scheme without clipping

Figure 9. Discretization error on a grid with 257^2 nodes along the vertical line $x = \frac{1}{2} - \frac{h_x}{4}$

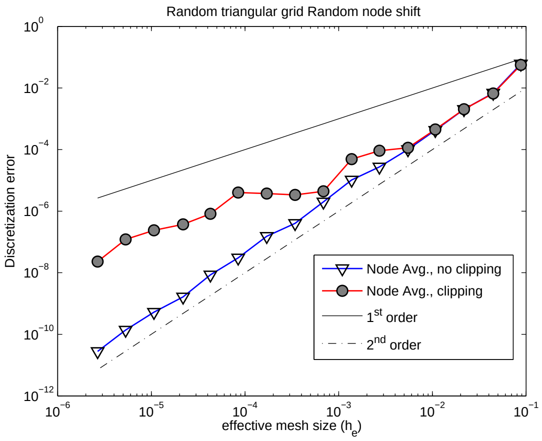

Figure 10. Downscaling test: discretization errors for NA schemes

β is a stretching factor, which is found from the condition $y_{N+1} = 1$. The stretching in the bottom half of the domain is defined analogously.

2. Irregularities are introduced by random shifts of nodes in the vertical and horizontal directions. The vertical shift is defined as $\Delta y_j = \frac{3}{16}\rho \min(h_y^{j-1}, h_y^j)$, where ρ is a random number between -1 and 1, and h_y^{j-1} and h_y^j are vertical mesh spacings on the background stretched mesh around the grid node. The horizontal shift is introduced analogously, $\Delta x_i = \frac{3}{16}\rho h_x$. With this random node perturbations, all perturbed quadrilateral cells are convex.

3. Each perturbed quadrilateral is randomly triangulated with one of the two diagonal choices; each choice has probability of one half.

An irregular random stretched grid with 65^2 nodes is presented in Figure 11(a). The manufactured solution is $U = \sin\left(\pi x + 2\pi y + \frac{\pi}{6}\right)$.

A recent study[5] assessed accuracy of gradient approximation on various irregular grids with high aspect ratio $A = \frac{h_y}{h_x} \gg 1$. Summary of the relevant results for grids of types (I)-(VI) is presented in Table 4. The study indicates

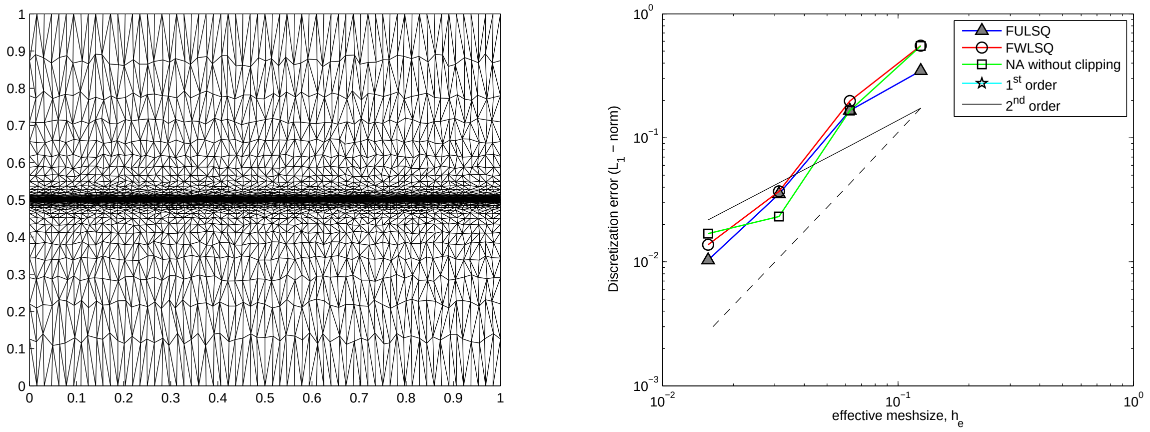

(a) Random triangular stretched grid with 65^2 nodes

(b) Discretization error (L_1 norm)

Figure 11. Convergence of cell-centered FVD schemes on stretched irregular triangular grids with discontinuous metrics

that for high-aspect-ratio grids and manufactured solutions significantly varying in the direction of large mesh spacing, the face-gradient reconstruction may produce extremely large relative errors (the relative errors are $O(Ah_x)$).

Table 4. Relative error of gradient reconstruction

Grids	(I)	(II)	(III)	(IV) –(VI)
NC	$O(h_x^2)$	$O(h_x^2)$	$O(h_x)$	$O(Ah_x)$
CC-NA	$O(h_x^2)$	$O(Ah_x^2)$	$O(Ah_x)$	$O(Ah_x)$
CC-FULSQ	$O(h_x^2)$	$O(Ah_x^2)$	$O(Ah_x)$	$O(Ah_x)$
CC-FWLSQ	$O(h_x^2)$	$O(Ah_x^2)$	$O(Ah_x)$	$O(Ah_x)$

A poor gradient reconstruction accuracy, however, does not necessarily imply large discretization error. Mavriplis[16] reported (second-order) accurate node-centered solutions even on grids with large gradient reconstruction errors. Here, we observe similar results for cell-centered formulations. Convergence of the L_1 norms of discretization errors on a sequence of consistently refined stretched grids with maximum aspect ratio $A = 1000$ is shown in Figure 11(b). Although somewhat erratic, all discretization errors are relatively small and converge in grid refinement with second order on average.

VIII. Grids with curvature and high aspect ratio

In this section, we discuss accuracy of FVD schemes on grids with large mesh deformations induced by a combination of curvature and high aspect ratio. The grid nodes are generated from a cylindrical mapping where (r, θ) denote polar coordinates with spacings of h_r and h_θ, respectively; the innermost radius is $r = R$. The grid aspect ratio is defined as the ratio of mesh sizes in the circumferential and the radial directions, $A = \frac{Rh_\theta}{h_r}$. The mesh deformation is characterized by the parameter Γ:

$$\Gamma = \frac{R\,(1-\cos(h_\theta))}{h_r} \approx \frac{Rh_\theta^2}{2h_r} = A\frac{h_\theta}{2}. \tag{14}$$

The following assumptions are made about the range of parameters: $R = 1$, $A \gg 1$, and $\Gamma h_r \ll 1$, which implies that both h_r and h_θ are small. For a given value of A, the parameter Γ may vary: $\Gamma \gg 1$ corresponds to meshes with large curvature-induced deformation; $\Gamma \ll 1$ indicates meshes that are locally (almost) Cartesian. In a mesh refinement that keeps A fixed, $\Gamma = O(Ah_\theta)$ asymptotes to zero. This property implies that on fine enough grids with fixed curvature and aspect ratio the discretization error convergence is expected to be the same as on similar grids generated on rectangular domains with no curvature.

We are focusing on difficulties specific to high-Γ grids with large curvature-induced deformations. The difficulties arise for functions that are predominantly varying in the radial direction of small mesh spacing. For functions predominantly varying in the direction of small mesh spacing, gradient reconstruction in rectangular geometries is expected to be accurate.[5]

Three types of 2D grids are considered for the cylindrical geometry: (I) *regular quadrilateral grids*; (II) *regular triangular grids* derived from the regular quadrilateral grids by the same diagonal splitting of each quadrangle; (III) *random triangular grids*, in which regular quadrangles are split by randomly chosen diagonals, each diagonal orientation occurring with probability of half. Grids of types (I) and (II) are regular; grids of type (III) are irregular because there is no periodic connectivity pattern. The grid types are shown in Figures 12. For a better visualization of the grid topology, low-Γ cylindrical grids are shown. Random node perturbation is not applied to high-Γ cylindrical grids because even small perturbations in the circumferential direction may lead to non-physical control volumes.

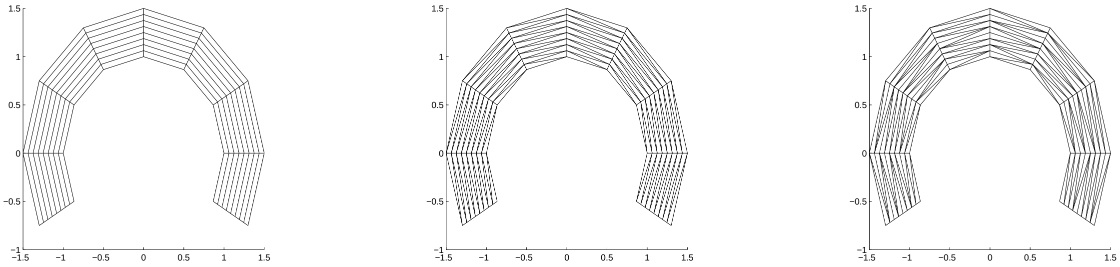

(a) Type (I): Regular quadrilateral grid (b) Type (II): Regular triangular grid (c) Type (III): Random triangular grid

Figure 12. Typical cylindrical grids.

A. Accuracy of gradient approximation

It was observed and confirmed analytically,[16,17,19] that the unweighted-least-square gradient approximation is zeroth order accurate on deformed grids with high Γ. Least square method with inverse-distance weighting has been proposed and shown to provide an accurate gradient approximation at nodes for node-centered formulations.

The study[5] shows that both FULSQ and FWLSQ methods suffer accuracy degradation on high-Γ grids. To improve the accuracy of gradient approximation, a least-square minimization in a mapped domain has been proposed. Two mapped least-square methods have been considered: an exact mapping (FEMLSQ) method that uses the polar coordinates directly; and a more general approximate mapping (FAMLSQ) method that is based on the distance function, defined as the distance to the nearest boundary, normally available in practical schemes. Applicability of FEMLSQ is limited to model problems with analytical boundary shape.

The more general FAMLSQ method approximates the FEMLSQ method by applying the least-square minimization in a locally constructed coordinate system.

$$f^r \equiv f_0 + \kappa\xi' + \lambda\eta'. \tag{15}$$

The local coordinates, (ξ', η'), are constructed using the distance function, which provides information on the closest boundary point. First the distance function is reconstructed at the face center. The coordinate vectors at the face center are defined as a unit η'-directional vector pointing in the direction opposite to the closest boundary point and its orthonormal ξ'-directional vector. The η'-coordinate is its distance from the boundary and the ξ'-coordinate is the projection of the vector connecting the stencil point with the face center onto the ξ'-direction. For the cylindrical geometry, the distance function is the shifted radial function, $r - R$. The gradient approximation accuracy for high-Γ grids of types (I)-(III) has been studied in[5] and is summarized in Table 5 . The least-square gradient reconstruction methods shown in the table use stencils of type (A), but the results are the same for stencils of type (B).

Table 5. High-Γ grids: relative errors of F-gradient reconstruction

	(I)	(II)	(III)
NC	$O(h_\theta^2)$	$O(h_\theta)$	$O(h_\theta)$
CC-FULSQ	$O(h_\theta^2)$	$O(1)$	$O(1)$
CC-FWLSQ	$O(h_\theta^2)$	$O(1)$	$O(1)$
CC-FEMLSQ	$O(h_r^2)$	$O(h_r^2)$	$O(h_r^2)$
CC-FAMLSQ	$O(h_\theta^2)$	$O(h_\theta^2)$	$O(h_\theta^2)$
CC-NA	$O(h_\theta^2)$	$O(h_\theta^2)$	$O(Ah_\theta)$

B. Discretization error convergence

Discretization errors of cell-centered schemes are compared with the errors of the node-centered scheme on a sequence of stretched high-Γ grids of type (III). The tests are performed for the manufactured solution $U = \sin(\pi r)$. The computational grids are derived from background regular cylindrical grids with the radial extent of $1 \le r \le 1.04$ and the angular extent of $10°$. The background grids have twice as many nodes in the radial direction than in the circumferential direction. The stretching performed in the radial direction provides a fixed maximal aspect ratio $A = 21817$ throughout the grid refinement study. The maximal value of parameter Γ changes approximately from 240 to 30. The stretching ratio is changing as $\beta = 1.94, 1.38, 1.175$, and 1.083. A representative 17×33 grid is shown in Figure 13(a).

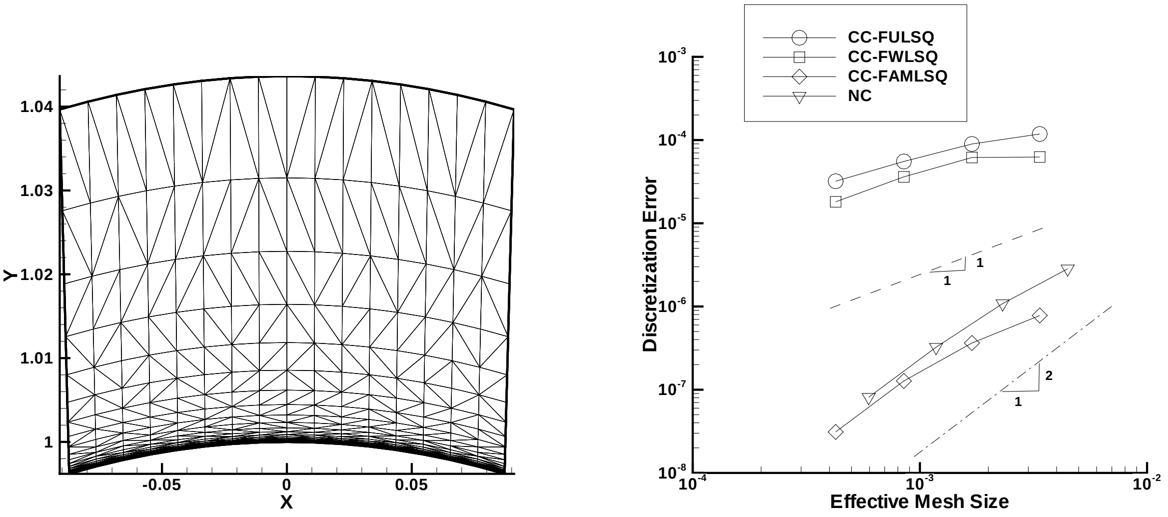

(a) High-Γ grid

(b) Discretization errors

Figure 13. Comparison of cell-centered and node-centered discretizations on high-Γ grids of type (III)

Convergence of the L_1-norm of the discretization errors is shown in Figure 13(b). The cell-centered (CC) least-square gradient reconstruction methods use stencils of type (A). The errors of the node-centered (NC) solution and the CC-FAMLSQ solution converge with second order and are almost over-plotted on fine grids indicating the same accuracy per degree of freedom. The errors of other two cell-centered least-square methods are significantly higher and appear convergent with first order. Inspection of the discretization stencils reveals that the NC stencil correctly reflects the strong coupling in the direction of small mesh spacing; the CC-FULSQ and CC-FWLSQ stencils fail to identify the strong coupling direction.

Least-square methods with compact stencils of type (B) for gradient reconstruction are better suited for high-aspect-ratio grids of types (II) and (III). Figure 14(b) shows convergence of cell-centered methods on a sequence of consistently refined stretched grids of type (III) with the radial extent $1 \leq r \leq 1.001$ and the angular extent of 10°. The fixed maximum aspect ratio is $A = 100,000$; $\Gamma \approx 550$ on the coarsest 9×17 grid and $\Gamma \approx 70$ on the finest 65×129. The stretching ratio is changing as $\beta = 1.57, 1.25, 1.11,$ and 1.055. The 17×33 grid is shown in Figure 14(a). The manufactured solution $U = \sin(2\pi r + \pi/6)$.

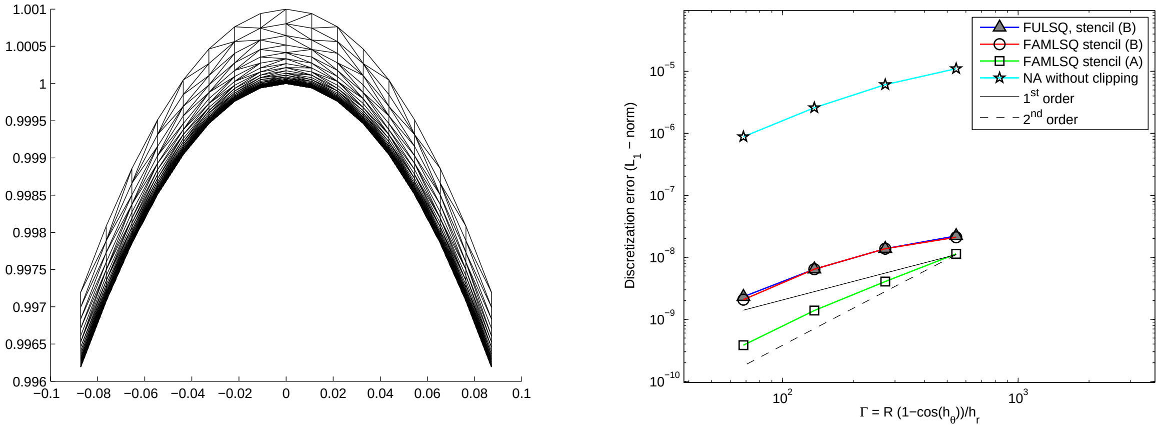

(a) High-Γ grid

(b) Discretization errors

Figure 14. Cell-centered discretizations on high-Γ grid of type (III)

Four cell-centered schemes are tested: the FULSQ scheme with compact stencils of type (B), the FAMLSQ schemes with stencils of types (A) and (B), and the NA scheme. Similar to the results of the previous tests (Figure 13(b)), the discretization errors of the FAMLSQ scheme with stencils of type (A) are the smallest. However, the errors of the FULSQ scheme with stencils of type (B) are not much larger, showing significant improvement over the least-square schemes with stencils of type (A). The discretization errors of the FAMLSQ scheme with stencils of type (B) are over-plotted with the FULSQ errors, indicating that the FULSQ convergence is optimal for the given stencil choice. The discretization errors of the NA scheme are several orders of magnitude higher than the errors of other schemes.

IX. Stability of defect-correction iterations for node-averaging schemes

In this section, we apply the local mode Fourier (LMF) analysis to analyze stability of defect-correction iterations on regular skewed grids of type (II). A sketch of a skewed grid is shown in Figure 15(a). The analysis is performed for a discrete Fourier test function $e^{j(\theta_x i_x + \theta_\eta i_\eta)}$, where (θ_x, θ_η) are normalized Fourier frequencies in the horizontal x-direction and in the skewed η-direction, respectively. Figure 15(a) illustrates the notation. For node-centered formulations, the Fourier symbol of the discrete operators is a scalar functional of the normalized frequencies; for cell-centered formulations, the symbol is a 2×2 matrix that couples Fourier components defined at the low and upper triangles.

Defect-correction iterations with the TSL driver are applied to the target NA scheme without clipping on grids with high skewing. The grid skew angle is defined as the maximum skew angle over all faces. The stability of iterations enhanced by the main-diagonal contributions from pseudo-time stepping characterized by the viscous CFL number. The results of the LMF analysis shown in Figure 15(b) demonstrate the relation between the maximum grid skew angle and the CFL number required for stability of the defect-correction iterations. The CFL number drops to two on grids with high skewing, effectively making the scheme explicit. The predictions of the LMF analysis have been precisely confirmed by numerical testing. Note that the CFL requirements for stability of defect-correction iterations for the NA scheme with clipping are exactly the same.

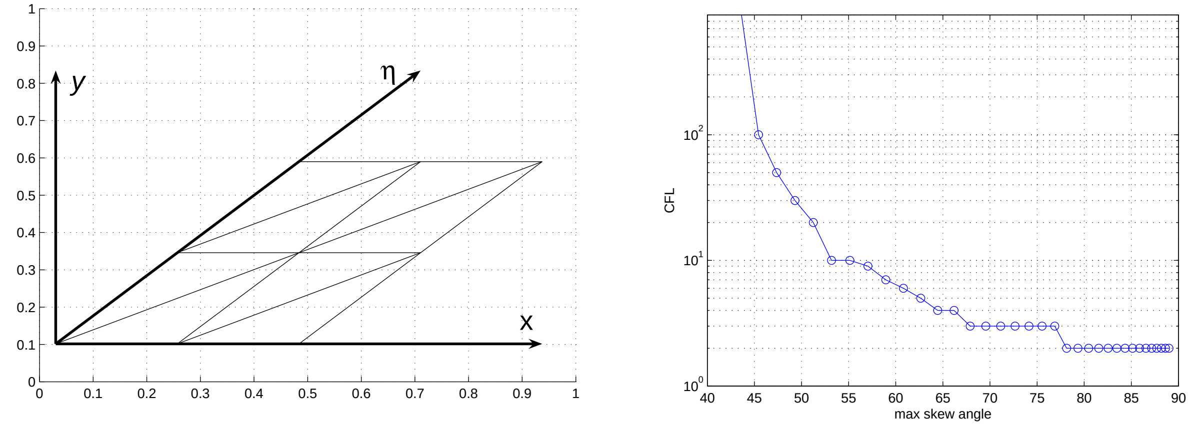

(a) Skewed grid of type (II)

(b) CFL vs. skew angle

Figure 15. Maximum viscous CFL number providing stability of defect-correction iterations on skewed grids of type (II). The driver operator is edge-based TSL scheme, the target operator is NA scheme without clipping.

X. Conclusions

Node-centered and cell-centered schemes are compared for finite-volume discretization of Poisson's equation as a model of the viscous flow terms. The comparisons are made for two classes of tests: the first class is representative of adaptive-grid simulations and involves irregular grids with discontinuous metrics; the second class is representative of high-Reynolds number turbulent flow simulations over a curved body.

Among the compared schemes, grids, and solutions, the node-centered scheme looks the most attractive. The scheme is known to deteriorate to first order for inviscid solutions on irregular mixed-element grids,[4,21] but for viscous terms, its accuracy is always second order and comparable with the accuracy of the best cell-centered schemes at equivalent number of degrees of freedom; also the linearization stencil of the node-centered scheme involves the least number of neighbors.

The cell-centered node-averaging (NA) scheme has three significant drawbacks. The first is that the NA scheme with clipping can fail to converge to the exact solution. Note, however, that the clipping is introduced mainly for stability of the inviscid solution and can be eliminated for the viscous terms. The second drawback is that the scheme demonstrates inferior accuracy on certain triangulated highly anisotropic grids in curved geometries. The third drawback is that the scheme's linearization stencil is quite large in comparison to the other schemes. Only the edge-based linearization terms are typically used for iterative solutions in a defect-correction setting. For high grid skewing, unavoidable in highly anisotropic triangular/tetrahedral grids used for high Reynolds number simulations, the scheme has explicit stability limitations.

The cell-centered schemes using least-square face gradient reconstruction have more compact stencils with a complexity similar to the complexity of the node-centered scheme. For the first class of tests representative of adaptive-grid simulations, the face least-square methods, the NA method without clipping, and the node-centered method demonstrate second-order convergence of discretization errors with very similar accuracies per degree of freedom. Accurate solutions have been obtained even for combinations of grid/manufactured-solution/scheme for which gradients are approximated with large relative errors. For simulations on highly anisotropic curved grids, the least-square methods have to be amended either by introducing a local mapping of the surface anisotropy or modifying the scheme stencil to reflect the direction of strong coupling.

References

[1] W. K. Anderson and D. L. Bonhaus, *An implicit upwind algorithm for computing turbulent flows on unstructured grids*, Computers and Fluids, 23 (1994), pp. 1–21.

[2] T. J. Barth, *Numerical aspects of computing high-Reynolds number flow on unstructured meshes*, AIAA Paper 91-0721, 29-th AIAA Aerospace Science Meeting, Reno, NV, January 1991.

[3] W. J. Coirier, *An adaptively-refined, cartesian, cell-based scheme for the Euler and Navier-Stokes equations*, tech. rep., NASA TM-106754, October 1994.

[4] B. Diskin and J. L. Thomas, *Accuracy analysis for mixed-element finite-volume discretization schemes*, tech. rep., NIA Report 2007-08, National Institute of Aerospace, August 2007.

[5] ———, *Accuracy of gradient reconstruction on grids with high aspect ratio*, tech. rep., NIA Report 2008-12, National Institute of Aerospace, December 2008.

[6] N. T. Frink, *Assesment of an unstructured-grid method for predicting 3-D turbulent viscous flows*, AIAA Paper 96-0292, 34-nd AIAA Aerospace Science Meeting and Exhibit, Reno, NV, January 1996.

[7] ———, *Tetrahedral unstructured navier-stokes methods for turbulent flows*, AIAA Journal, 36 (1998), pp. 1975–1982.

[8] M. B. Giles, *Accuracy of node-based solutions on irregular meshes*, in 11-th International Conference on Numerical Methods in Fluid Dynamics, D. L. Dwoyer, M. Y. Hussaini, and R. Voigt, eds., Lecture Notes in Physics, v. 323, Springer-Verlag, 1989, pp. 369–373.

[9] A. C. Haselbacher, *A Grid-Tranparent Numerical Method for Compressible Viscous Flow on Mixed Unstructured Meshes*, PhD thesis, Loughborough University, 1999.

[10] ———, *On constrained reconstruction operators*, AIAA Paper 2006-1274, 44-th AIAA Aerospace Science Meeting and Exhibit, Reno, NV, January 2006.

[11] A. C. Haselbacher, J. J. McGuirk, and G. J. Page, *Finite-volume discretization aspects for viscous flows on mixed unstructured grids*, AIAA Journal, 37 (1999), p. 477.

[12] C. Hirsch, *Numerical computation of internal and external flows. Vol.1, Fundumentals of numerical discretization*, A Wiley-Interscience publication, John Wiley & Sons, Inc., 605 Third Avenue, New York, NY 10158-0012, USA, 1988.

[13] D. G. Holmes and S. D. Connell, *Solution of the 2D Navier-Stokes equations on unstructured adaptive grids*, AIAA Paper 89-1392, 9-th AIAA CFD conference, Washington, DC, June 1989.

[14] D. R. Lindquist and M. B. Giles, *A comparison of numerical schemes on triangular and quadrilateral meshes*, in 11-th International Conference on Numerical Methods in Fluid Dynamics, D. L. Dwoyer, M. Y. Hussaini, and R. Voigt, eds., Lecture Notes in Physics, v. 323, Springer-Verlag, 1989, pp. 273–277.

[15] T. A. Manteuffel and A. B. White, *The numerical solution of the second-order boundary value problem on nonuniform meshes*, Mathematics of Computations, 47(176) (1986), pp. 511–536.

[16] D. J. Mavriplis, *Revisiting the least-square procedure for gradient reconstruction on unstructured meshes*, AIAA Paper 2003-3986, 18-th AIAA CFD conference, Orlando, FL, June 2003.

[17] N. V. Petrovskaya, *The choice of weight coefficients for least-square gradient approximation*, J. Math. Mod., 16(5) (2004), pp. 83–93. (in Russian).

[18] R. D. Rausch, J. T. Batina, and H. T. Yang, *Spatial adaptation procedures on unstructured meshes for accurate unsteady aerodynamic flow computation*, AIAA Paper 89-1392, 9-th AIAA CFD conference, Washington, DC, June 1989.

[19] T. M. Smith, M. F. Barone, R. B. Bond, A. A. Lorber, and D. G. Baur, *Comparison of reconstruction techniques for unstructured mesh vertex centered finite volume scheme*, tech. rep., 18-th AIAA CFD Conference, Miami, FL, June 2007. AIAA Paper 2007-3958.

[20] A. Syrakos and A. Goulas, *Estimate of the truncation error of finite volume discretization of the Navier-Stokes equations on collocated grids*, Int. J. Numer. Meth. Fluids, 50 (2006), pp. 103–130.

[21] J. L. Thomas, B. Diskin, and C. L. Rumsey, *Towards verification of unstructured-grid solvers*, AIAA Journal, 46 (2008), pp. 3070–3079.

[22] E. Turkel, *Accuracy of schemes with nonuniform meshes for compressible fluid flows*, Applied Numerical Mathematics, 2 (1986), pp. 529–550.